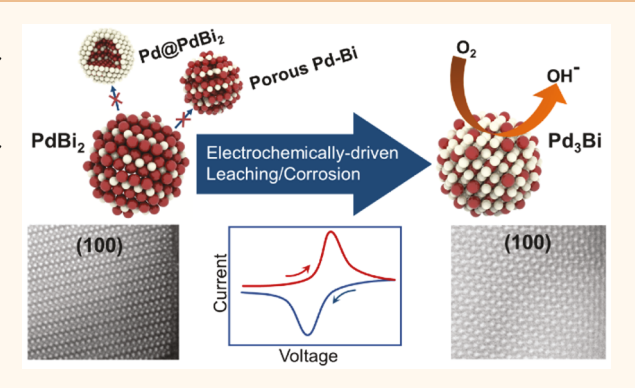


Ordered Intermetallic Pd₃Bi Prepared by an **Electrochemically Induced Phase** Transformation for Oxygen Reduction **Electrocatalysis**

Du Sun, † Yunfei Wang, † Kenneth J.T. Livi, † Chuhong Wang, † Ruichun Luo, † Zhuoqun Zhang, † Hamdan Alghamdi, * Chenyang Li, † Fufei An, † Bernard Gaskey, † Tim Mueller, † and Anthony Shoji Hall*,†

Supporting Information

ABSTRACT: The synthesis of alloys with long-range atomicscale ordering (ordered intermetallics) is an emerging field of nanochemistry. Ordered intermetallic nanoparticles are useful for a wide variety of applications such as catalysis, superconductors, and magnetic devices. However, the preparation of nanostructured ordered intermetallics is challenging in comparison to disordered alloys, hindering progress in material development. Herein, we report a process for converting colloidally synthesized ordered intermetallic PdBi, to ordered intermetallic Pd₃Bi nanoparticles under ambient conditions by electrochemical dealloying. The low melting point of PdBi2 corresponds to low vacancy formation energies, which enables the facile removal of the Bi from the surface while



simultaneously enabling interdiffusion of the constituent atoms via a vacancy diffusion mechanism under ambient conditions. The resulting phase-converted ordered intermetallic Pd₃Bi exhibits 11 times and 3.5 times higher mass activity and high methanol tolerance for the oxygen reduction reaction compared with Pt/C and Pd/C, respectively, which is the highest reported for a Pd-based catalyst, to the best of our knowledge. These results establish a key development in the synthesis of noble-metal-rich ordered intermetallic phases with high catalytic activity and set forth guidelines for the design of ordered intermetallic compounds under ambient conditions.

KEYWORDS: oxygen reduction reaction, palladium, ordered intermetallic, bismuth, phase conversion, electrocatalysis, dealloying

oble-metal-rich phases of alloys have recently emerged as high-performance catalysts for a variety of industrially relevant catalytic applications. The mixing of two different metals can result in a solid solution that exhibits short-range ordering of atoms (disordered alloy) or an ordered intermetallic that exhibits both short-range and long-range ordering of atoms. Ordered intermetallic compounds (OICs) can have superior catalytic performance and stability compared with disordered alloys because of the atomically uniform active sites provided by long-range structural periodicity and stronger interatomic bonding from a more negative enthalpy of mixing. $^{1-7}$

OICs are difficult to prepare, often requiring annealing to temperatures of ~700 °C to facilitate interdiffusion and

equilibration of atoms. The direct synthesis of some ordered intermetallic nanostructures has been achieved at a relatively mild temperature by using harsh reducing agents, special reaction parameters such as microwave or solvothermal conditions, or electrochemical deposition. 7-10 Moreover, noble-metal-rich phases (>50% noble metal) are particularly challenging to synthesize under mild conditions, even if the ordered phases are thermodynamically favored, given the high melting points of the noble metals and the low diffusion rates in crystal lattices that inhibit equilibration.^{6,11}

Received: July 30, 2019 Accepted: August 30, 2019 Published: August 30, 2019



[†]Department of Materials Science and Engineering, Johns Hopkins University, Baltimore, Maryland 21218, United States [‡]School of Materials Science and Engineering, Shanghai Jiao Tong University, Shanghai 200030, P. R. China

[§]Department of Chemical and Biomolecular Engineering, Johns Hopkins University, Baltimore, Maryland 21218, United States

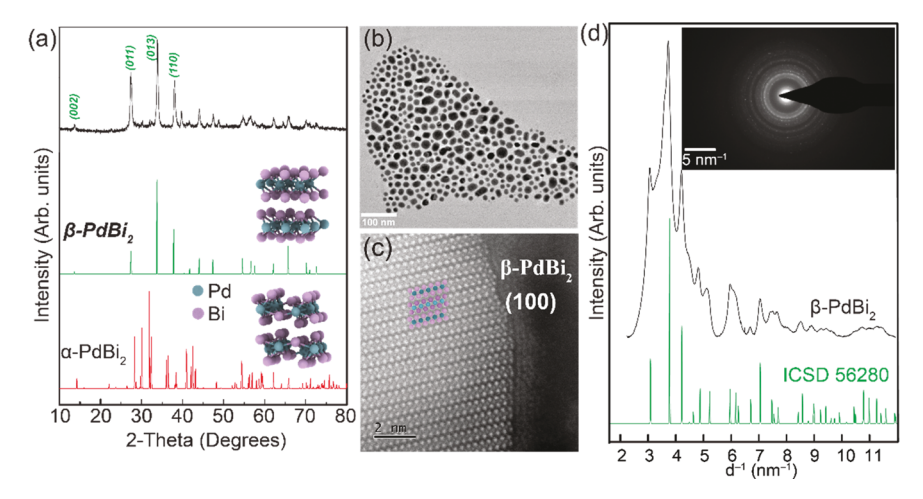


Figure 1. (a) Powder X-ray diffraction pattern of the as-prepared sample. The crystal planes that belong to α -PdBi₂ are marked in red, whereas the ones for β -PdBi₂ are in green. (b) TEM shows a representative image of the as-prepared nanoparticles. (c) STEM-HAADF image reveals the atomic arrangement of the nanoparticles. The atoms match with the (100) plane of β -PdBi₂. (d) Line plot of intensity versus reciprocal lattice spacing derived from the rotationally averaged SAED pattern shown in the inset (black) and simulated β -PdBi₂ (green) ICSD 56280.

The preparation of highly dispersed OIC catalysts by annealing at high temperatures is challenging because sintering occurs during annealing, reducing the surface area to volume ratio. The most common method for reducing sintering is to physically isolate the particles by encapsulation with a template before annealing. After crystallization, the templates can be chemically etched away. 12–14 The ability to control the shape of the particle is lost because the most thermodynamically stable facet is typically expressed from surface reconstructions that occur during the phase transformation.¹⁵ Additionally, contamination can occur at elevated temperatures because this can allow atoms from the support or template to diffuse into the alloy. The preparation of catalytically active OIC nanostructures under mild conditions remains a great challenge in catalysis science. Studies focusing on methods for the preparation of OIC nanoparticles (NPs) are limited in comparison with those focusing on disordered alloys. If OICs are to be practically utilized for devices, then methods that allow the preparation of OIC NPs under ambient conditions are needed.

It is known in the corrosion literature that the atoms of alloys with low melting points exhibit high diffusivity during dealloying at room temperature. $^{16-19}$ In contrast, materials with high melting points (mp >1000 °C) have low diffusivity; during dealloying, a thin noble-metal film will form over the surface, protecting the surface against further dealloying across a wide range of voltages. This has been observed in bulk alloys such as Cu–Pd, Cu–Au, and so on and on NP alloys in which a noblemetal shell forms over the alloy cores in systems such as Pt₃Co, Cu₃Pt, Pt₃Ni, FeAu, and so on. $^{4,16,17,20-22}$ From these design principles, it can be inferred that the controlled corrosion of a non-noble element from a low-melting-point alloy NP could permit the conversion to a noble-metal-rich OIC. 18,19

Here we validate this concept by illustrating the kinetically controlled conversion of ordered intermetallic $PdBi_2$ (mp \sim 480 °C) NPs to ordered intermetallic Pd_3Bi NPs via electrochemical dealloying at room temperature. The low melting point of $PdBi_2$ indicates that it has low-vacancy formation energies, which enables the facile removal of the Bi from the surface while simultaneously enabling interdiffusion of the constituent atoms via a vacancy diffusion mechanism at room temperature. This method allows for the entire particle to reconstruct to a noble-metal-rich OIC phase that has never been prepared under

ambient conditions. The phase-converted Pd_3Bi exhibits recordbreaking mass activity for the oxygen reduction reaction (ORR), reaching activities as high as 1.2 A mg_{Pd}^{-1} at 0.9 V versus the reversible hydrogen electrode (RHE), which is ~3.4 times higher than Pd/C and 11 times higher than Pt/C, respectively.

RESULTS AND DISCUSSION

Synthesis and Characterization of PdBi₂. The PdBi₂ nanostructures were synthesized by the reduction of Pd(II) acetylacetonate and Bi(III) acetate in oleylamine at 300 °C. PdBi₂ has two known layered phases, denoted as and β -PdBi₂ and α -PdBi₂. The peaks in the experimental X-ray diffraction (XRD) pattern exhibit broadening (Figure 1a), suggesting that the crystallite size is on the nanoscale. The pattern can be indexed to β -PdBi₂ with a small amount of α -PdBi₂. The (011) deflection is more intense in synthesized PdBi₂ than the simulated pattern, indicating the preferential orientation along this direction. Note that there is a shift of some of the peaks, which may be caused by surface tension; this is commonly seen in nanomaterials with small crystallites. ^{28,29}

The morphology and crystalline phases of $PdBi_2$ were probed by high-resolution transmission electron microscopy (HRTEM). The sizes of the $PdBi_2$ particles ranged from ~ 10 to 50 nm in diameter (Figure 1b and Figure S1). The particles have a core—shell structure where the core is single-crystalline and the shell is amorphous (Figure 1c). The atomic arrangement of the core matches the (100) plane of β -PdBi₂, and the amorphous shell is Bi (Figure S2). The selected area electron diffraction (SAED) is presented as a 1D line plot (Figure 1d) and compared with the 1D diffraction pattern of β -PdBi₂. Both patterns match well, indicating that the crystalline phases present in the material are β -PdBi₂.

Electrochemical Phase Conversion of PdBi₂. To interrogate the stability of PdBi₂, we cycled the material from 0.1 to 1.1 V vs RHE (henceforth all potentials will be reported versus this reference electrode) under O₂ at 1600 rpm in 0.1 M KOH. Two redox waves appear between ~0.5 and 0.75 V in the ORR voltammogram, indicating that a background corrosion process occurs in parallel with the ORR (Figure S3a). Upon repeated potential cycling, the activity continuously increases, and redox waves decrease, finally reaching stability after ~500 cycles. The features in the cyclic voltammograms (CVs) collected under Ar

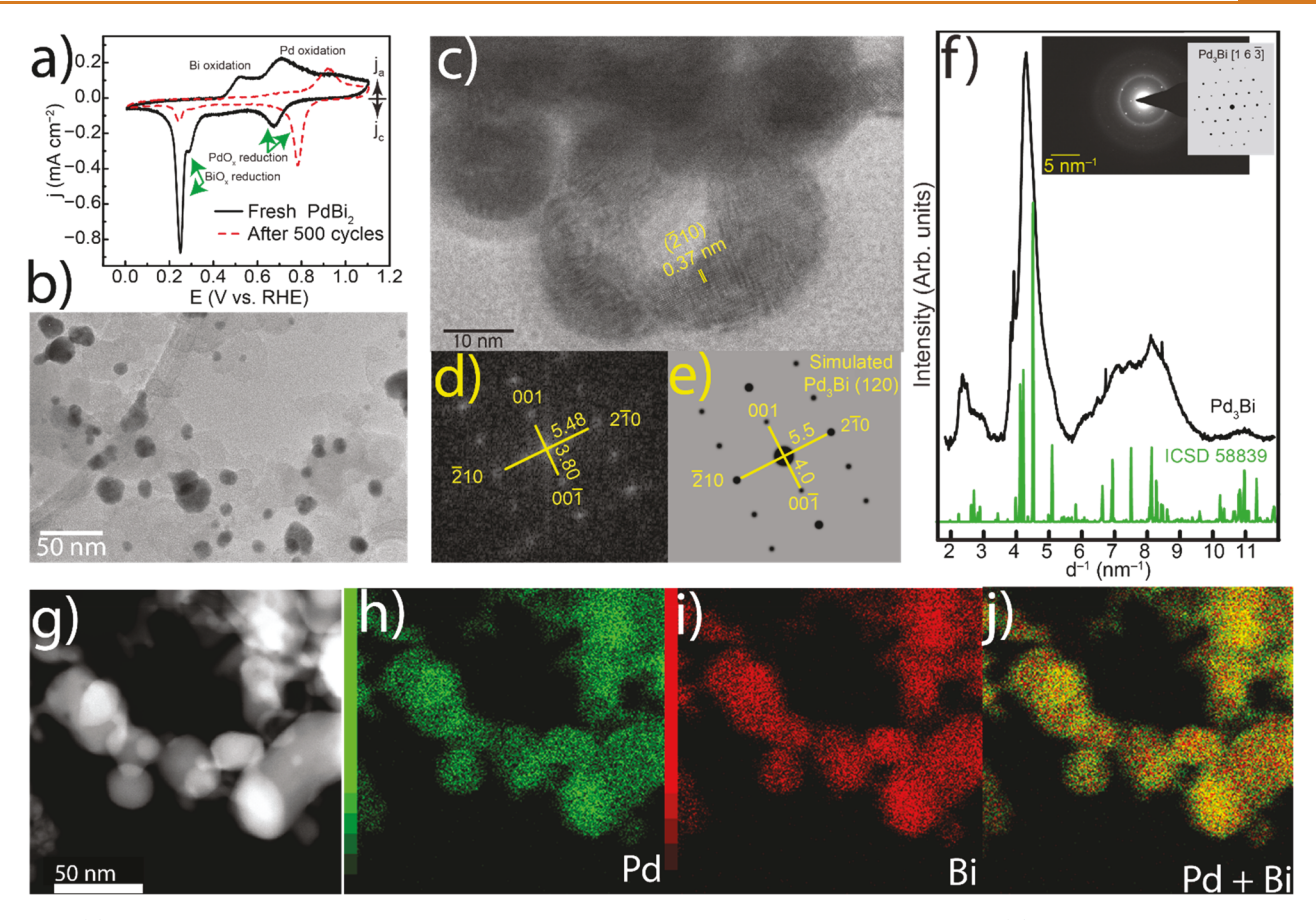


Figure 2. (a) CVs of the $PdBi_2$ in Ar-saturated 0.1 M KOH before and after the electrochemical dealloying. (b) TEM image of dealloyed- $PdBi_2$ supported on Vulcan carbon, demonstrating that aggregation can be suppressed. (c) HRTEM image of $PdBi_2$ after conversion and (d) its corresponding FFT pattern, (e) which matches with the simulated Pd_3Bi down the [120] direction. (f) Line plot of intensity versus reciprocal lattice spacing derived from the rotationally averaged SAED pattern shown in the inset (black) and simulated Pd_3Bi (green) ICSD 58839. (g) HAADF-STEM image of $PdBi_2$ after conversion and its corresponding EDS map of (h) Pd, (i) Pd, (i) Pd, and (j) Pd and Pd all reciprocal distances in panels d and e are in units of $PdBi_2$ after conversion and $PdBi_2$ after conversion and

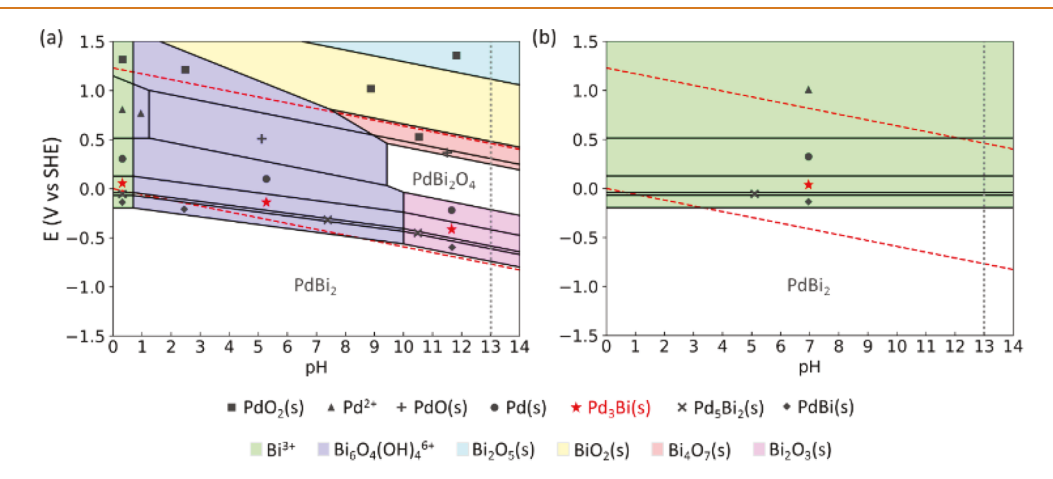


Figure 3. (a) Calculated Pd—Bi Pourbaix diagram. (b) Pourbaix diagram with oxides removed, so that dissolved Bi only forms aqueous Bi³⁺. Two-phase regions are marked with a color and a symbol. The colors indicate the equilibrium Bi oxide or solvated Bi-containing ion, and the symbols indicate the equilibrium phase that contains Pd. Single-phase regions are shaded white. The dashed red lines indicate the electrochemical stability window for water, with the lower line corresponding to 0 V vs RHE. The experimental pH of 13 is marked by a dotted gray line.

change significantly before and after cycling, indicating a change in surface structure of $PdBi_2$ (Figure 2a). The loss of intensity of Bi-related surface redox waves and a cathodic shift of Pd surface redox waves indicate that the surface of $PdBi_2$ is enriched with Pd. The BiO_x reduction feature at ~ 0.25 V is caused by a small

amount of residual Bi in the sample. The absence of hydrogen underpotential deposition (H-UPD) from 0 to 0.4 V indicates that the surface does not evolve to pure Pd but rather a Pd-rich alloy.

To assess the evolution of this structural change, we performed TEM after cycling (Figure 2b,c and Figure S4). Carbon-supported PdBi₂ NPs were dealloyed, and the resulting material displays isolated NPs which homogeneously decorate the carbon support, indicating that room-temperature processing can inhibit coarsening when the particles are spatially separated (Figure 2b). The dealloyed particles can form aggregates in the absence of the carbon supports because the particles are in direct contact during conversion (Figure 2c,g). Single-crystalline particles were observed, and the fast Fourier transform (FFT) pattern matches with the simulated electron diffraction pattern of Pd₃Bi along the [120] direction (Figure 2c-e). SAED patterns were acquired on an ensemble of particles and are presented as a 1D line scan (Figure 2f). The SAED line plots of electrochemically etched PdBi2 and simulated Pd3Bi match well. Within the SAED pattern, both a ring and spot pattern are observed, indicating that the region probed consists of both polycrystalline materials and single-crystalline materials. The spot pattern in the inset of Figure 2f matches well with the simulated electron diffraction pattern of Pd₃Bi along the $[16\overline{3}]$ direction. The atomic ratio of Pd and Bi after conversion was acquired by X-ray photoelectron spectroscopy (XPS) and inductively coupled plasma mass spectrometry (ICP-MS) (Figure S5 and Table S1). Both indicate a Pd/Bi atomic ratio of ~77:23% which corroborates well with the composition of the observed crystal structure of Pd₃Bi. High-angle annular darkfield-scanning transmission electron microscopy (STEM-HAADF) with energy-dispersive X-ray spectroscopy (EDS) mapping indicates that the Pd and Bi were mixed homogeneously throughout the particles (Figure 2g-j.) Taken together, these data indicate that PdBi₂ NPs convert to Pd₃Bi NPs (henceforth, denoted as converted Pd₃Bi) by electrochemical dealloying.

Electrochemical Stability of Phases. The removal of Bi from PdBi₂ upon cycling is consistent with the calculated Bi–Pd Pourbaix diagram (Figure 3a). In 0.1 M KOH solution (pH 13), PdBi₂ is predicted to become thermodynamically unstable above 0.03 V vs RHE. Under equilibrium conditions, as the voltage increases, Bi will dissolve from PdBi₂ to produce Bi₂O₃, leaving behind PdBi, then Pd₅Bi₂, then Pd₃Bi, before finally converting to Pd and Bi₂O₃ above 0.35 V vs RHE. The experimental observation of converted Pd₃Bi after cycling up to 1.1 V vs RHE indicates that the Pd₃Bi is kinetically stabilized. 30

The kinetic stabilization may be due to the slow formation of oxides upon Bi dissolution; for example, Bi₂O₃ is known to precipitate slowly from solutions of Bi^{3+,31} If the formation of oxides such as Bi₂O₃ is kinetically hindered and the conversion to Pd is assumed to proceed via the increase in the concentration of aqueous Bi³⁺ (Figure 3b) or BiOH²⁺ (Figure S6) ions, then Pd₃Bi can be expected to persist up to approximately 0.90 or 0.67 V, respectively, vs RHE. The formation of surface oxides on the NPs may further contribute to their kinetic stability. Moreover, the formation of crystalline Pd shells over Pd₃Bi cores (orthorhombic lattice) may also be kinetically hindered as the crystal structure and lattice constants vary considerably from the ground state of elemental Pd (FCC). Taken together, these data indicate that Pd₃Bi is kinetically stable and forms by a combination of Bi corrosion from PdBi₂ and atomic restructuring.

To probe the evolution of Pd_3Bi from $PdBi_2$, we collected high-resolution TEM images on a sample that was not transformed to completion (Figure 4). The image displays particles with a crystalline core and an amorphous shell.

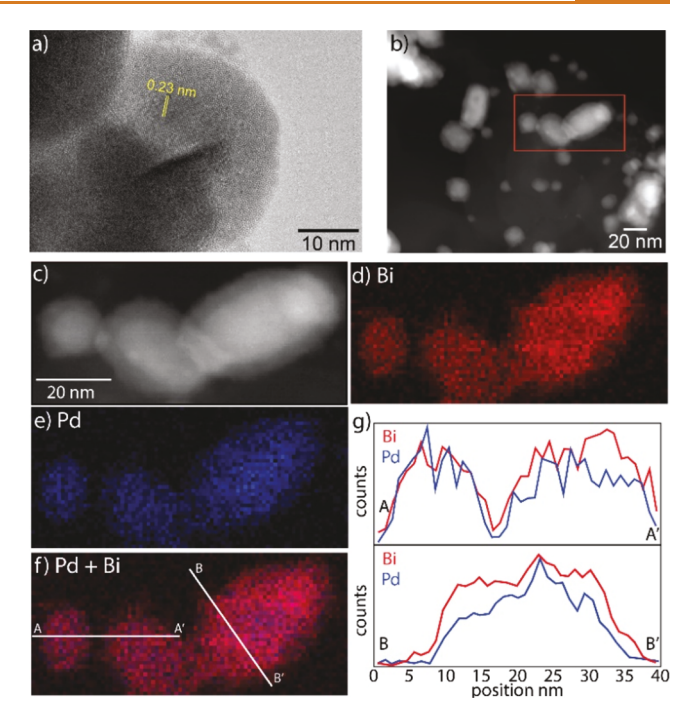


Figure 4. (a) TEM image of PdBi₂ after 200 cycles. The crystalline core is crystalline with a lattice constant of 0.23 nm, whereas the shell is amorphous. (b) HAADF-STEM images of PdBi₂ after 200 cycles, indicating that the crystalline core is denser than the amorphous shell. The large low-density particles in the background are Vulcan carbon. (c) HAADF-STEM imaging of the region in panel b highlighted in the red box. EDS mapping of (d) Bi, (e) Pd, and (f) Bi + Pd. (g) EDS line scans of the regions shown in panel f.

HAADF-STEM imaging indicated that the crystalline cores of the particles were denser than the amorphous shells (Figure 4b,c), and EDS mapping indicated that the atomic ratio (Pd/Bi) of the crystalline core is 1.08 ± 0.19 and that of the shell is $0.84 \pm$ 0.05 (2 σ). EDS mapping of Pd and Bi and line scans of the elemental composition of the particles shown in Figure 4c indicate that the shells of the particles are slightly richer in Bi than the cores (Figure 4d-g). Taken together, these data indicate that the removal of Bi from the surface of the particle leaves behind a defect-rich amorphous material that allows the facile transport of Bi out of the core, whereas the core reconstructs to a crystalline intermetallic phase. This observation is consistent with our prediction from the Pourbaix diagram that as Bi dissolves from PdBi2, intermetallic phases that are more Pd-rich are left behind as the particle is finally converted to Pd₃Bi.

Mobility of Atoms During Corrosion. To investigate the rate of phase conversion between the ordered intermetallic phases, we used density functional theory³² to calculate the minimum diffusion activation energy of Bi atoms in PdBi₂, assuming a vacancy-mediated diffusion mechanism. Minimum energy paths and saddle-point energies were determined with the climbing image nudged elastic band method.^{33,34} To identify possible paths, we have taken into account all possible jumps between an atom and a vacant neighboring site. The lowest barrier for Bi diffusion in PdBi₂ is 0.44 eV, corresponding to a 2D migration pathway (Figure S7). The mean-square displacement of a particle undergoing a 2D random walk via a vacancy-mediated mechanism is $\langle \Delta r^2 \rangle = 4x_{\nu}\Gamma a^2t$, where x_{ν} is the vacancy concentration, Γ is the hopping frequency from a filled to a vacant site, a is the hopping length, and t is the time. We estimate

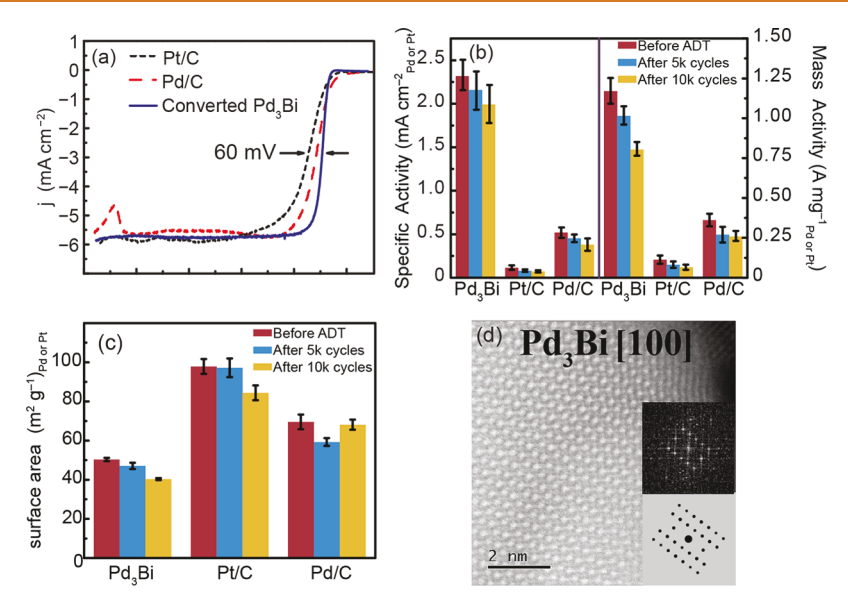


Figure 5. (a) Linear sweep voltammograms of Pt/C, Pd/C, and converted Pd₃Bi in O₂-saturated 0.1 M KOH. (b) Mass activity and specific activity at 0.9 V vs RHE before and after the stability test calculated from the Kouteký–Levich equation. Negative values indicate that the current is cathodic. (c) ECSA and mass loading before and after the stability test. ECSA was measured by CO stripping, and the mass loading was measured by ICP-MS. (d) STEM-HAADF image of a Pd₃Bi catalyst particle after 10 000 cycles of ADT. Inserts are the FFT of the image and the simulated single-crystal diffraction pattern down the [100] direction of Pd₃Bi, respectively. All voltammetry was collected on a 5 mm diameter RDE at 1600 rpm and a voltage sweep rate of 20 mV s⁻¹. The mass loading of all samples onto the 5 mm glassy carbon disk was between ~13 and 15 μ g_{Pd or Pt} cm₂co⁻².

the vacancy concentration using $x_{\nu} \approx \exp(-E_{\rm f}/k_{\rm B}T)$, where $E_{\rm f}$ is the vacancy formation energy. We find that diffusion of Bi through PdBi₂ is likely facilitated by high vacancy concentrations, as the calculated vacancy formation energy for Bi along the diffusion path is only 0.17 eV relative to bulk Bi. The vacancy formation energy will therefore be even lower relative to states in which the chemical potential of Bi is lower than that of bulk Bi, such as those that are predicted to be stable at higher potentials (Figure 3). This low calculated vacancy formation energy is consistent with the low melting point of PdBi₂. Transition-state theory 35 gives us $\Gamma \approx \nu^* \exp(-E_a/k_BT)$, where ν^* is generally in the range of phonon frequencies and E_a is the activation energy for a single hop. Using the reported vibrational frequency of ~ 10^{12} Hz for Bi in β -PdBi₂³⁶ we estimate that at room temperature the root-mean-square displacement of Bi in PdBi₂ reaches a typical particle width in well under 1 s. This result indicates that Bi diffusion in PdBi2 is facile, supporting the potential for the fast removal of Bi from PdBi2 under experimental conditions.

ORR Activity and Stability of Converted Pd₃Bi. The ORR activity of the converted-Pd₃Bi was compared with that of commercial Pt/C (TKK, 40% Pt on high surface area carbon) and Pd/C (Premetek, 40% Pd on Vulcan XC-72) catalysts (Figure 5a and Figure S7). The onset potential (the potential in which the current exceeds the background by 10%) of the ORR on Pt/C was 1.0 V and on Pd/C was 1.05 V, which agreed with literature reports,³⁷ whereas the converted Pd₃Bi was more negative (~ 0.97 V). At potentials more positive than the onset potential, the Pd and Pt sites are covered with a surface oxide, rendering them catalytically inactive. At more negative potentials (starting at ~0.95 V), we observed a rapid increase in the current of the converted Pd₃Bi, whereas the current for Pd/C and Pt/C increased gradually. The half-wave potential of converted Pd₃Bi was more positive by 60 and 32 mV relative to Pt/C and Pd/C, respectively, indicating that it may possess superior catalytic activity relative to the commercial catalysts.

The Koutecký-Levich (K-L) plot was constructed by measuring the steady-state current density at a constant voltage at various rotation rates to calculate the kinetic current density (Figures S9 and S10). The specific activity (SA) and mass activity (MA) were measured by normalizing the kinetic current density to the ECSA (Figure S11) or to the total mass of precious metal, respectively. The SA of converted Pd₃Bi was 2.3 $\pm 0.19 \text{ mA/cm}_{Pd}^2$ at 0.9 V vs RHE, which is 19 times higher than that of Pt/C $(0.12 \pm 0.03 \text{ mA/cm}_{Pt}^2)$ and 4.4 times higher than that of Pd/C $(0.52 \pm 0.07 \text{ mA/cm}_{Pd}^2)$ (Figure 5b). The MA of converted Pd₃Bi was 1.2 \pm 0.08 A mg_{Pd}⁻¹, which is 3.4 times higher than that of Pd (0.36 \pm 0.04 A mg_{Pd}⁻¹) and 11 times higher than that of Pt (0.11 \pm 0.02 A mg_{Pt} $^{-1}$) (Figure 5b). 6 The SA and MA of Pd₃Bi are among the highest reported for the alkaline ORR (Table S2). Remarkably, Pd3Bi exhibits a high MA despite a relatively modest specific surface area (Figure 5C), indicating that a decrease in particle size (increase in specific surface area) could permit even higher mass activities.

We evaluated the stability of our catalysts by performing accelerated durability testing (ADT) by cycling the samples from 0.6 to 1.0 V at a sweep rate of 100 mV/s. Converted Pd₃Bi retained 86 and 69% of the initial SA and MA, respectively, after 10 000 cycles at 0.9 V, whereas the specific surface area decreased by 20% (Figure 5b,c and Figure S11). In comparison, Pd/C retained 73 and 71% of the initial SA and MA, respectively, and Pt/C retained 63 and 54% of the initial SA and MA, respectively (Figure 5b). The specific surface area of Pt/C and Pd/C decreased by 14 and 3%, respectively. This indicates that the decreases in catalytic activity of the commercial samples were predominately caused by the removal of highly active sites by surface reconstructions or Ostwald ripening (Figure S13).³⁸ The decrease in activity for Pd₃Bi was coincident with the emergence of Ostwald ripening, as indicated by a decrease in the specific surface area and the emergence of a small amount of metallic Pd. The metallic Pd probably formed via the redeposition of dissolved Pd ion onto the electrode, as

evident from the appearance of H-UPD in the CVs collected under Ar after the ADTs (Figure S13, Figure 5c, and Table S2). This was further supported by ICP-MS and XPS (Table S3), which showed that the composition of the electrode was ~78% Pd and ~22% Bi after 10 000 cycles, indicating a 1% higher Pd content relative to the freshly converted samples. STEM-HAADF images of the sample after ADT confirmed that the particles retained intermetallic crystallinity (Figures 5d and Figure S5). Taken together, the data indicate that the corrosion of Pd₃Bi to Pd was kinetically slow, and hence it was able to sustain performance after 10 000 cycles, even outperforming freshly prepared Pt/C and Pd/C.

Fuel crossover and poisoning of the cathode, where the ORR takes place, drastically decreases the activity and durability of commercial direct methanol fuel cells. ^{39,40} This is largely due to the high catalytic activity of Pt and Pd for alcohol oxidation; ⁴¹ when fuel crosses over from the anode to the cathode, the cathode experiences a mixed potential from both oxidation and reduction reactions taking place simultaneously, eroding the current density and voltage of the device. To examine the tolerance of converted Pd₃Bi toward fuel crossover, we measured the ORR activity in the presence of methanol. The ORR performance of Pt/C, Pd/C, and converted Pd₃Bi in O₂-saturated 0.5 M CH₃OH + 0.1 M KOH was measured (Figure 6). Pd/C and Pt/C showed a significant increase in the

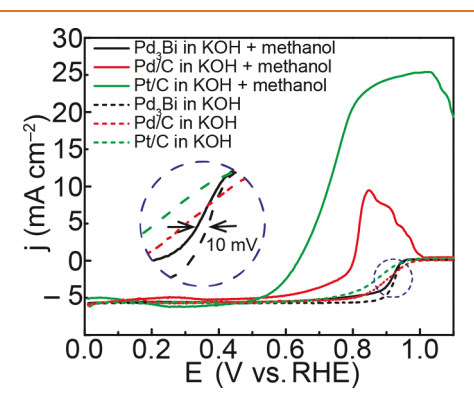


Figure 6. Linear sweep voltammograms of converted Pd₃Bi, Pd/C, and Pt/C in O₂-saturated 0.1 M KOH + 0.5 M CH₃OH. Rotation rate: 1600 rpm. Sweep rate: 20 mV s⁻¹. The mass loading of all samples onto the 5 mm glassy carbon disk was between ~13 and 15 μ g_{Pd or Pt} cm⁻²_{geo}.

overpotential for the ORR in the presence of methanol due to the competitive methanol oxidation over the ORR. The anodic peak at 1.02 V for Pt/C and the 0.85 V peak for Pd/C are from the oxidation of methanol, suggesting that the ORR is largely suppressed by the competing reaction. However, only a small 10 mV decrease in the $E_{1/2}$ for the ORR on converted Pd₃Bi is observed. This suggests that the converted Pd₃Bi has superior methanol tolerance and is a promising cathode catalyst for direct methanol fuel cells. ⁴²

CONCLUSIONS

We have demonstrated kinetically controlled corrosion as an effective approach to convert base-metal-rich ordered intermetallic NPs $(PdBi_2)$ to catalytically active ordered intermetallic NPs (Pd_3Bi) at room temperature and atmospheric pressure. We have employed the converted Pd_3Bi NPs as electrodes for the ORR with high methanol tolerance. The resulting material exhibited superior MA relative to commercial Pd/C and Pt/C.

We found that a low-melting-point-ordered intermetallic NP can convert to a noble-metal-rich ordered intermetallic NP with high catalytic activity due to the facile formation of vacancies and the high mobility of interdiffusion. This strategy opens a synthetic method for accessing high-performance heterogeneous catalysts under ambient conditions.

EXPERIMENTAL METHODS

Materials. Palladium(II) acetylacetonate (Pd(acac)2, 99%, Strem Chemicals), bismuth(III) acetate (Bi(oac)3, 99.99%, Alfa Aesar), oleylamine (OLAM, technical, 70%, Aldrich), 40% Pd on Vulcan XC-72 (Premetek), O_2 gas (UHP grade, Airgas), and 40% Pt on high-surface-area carbon (TEC10E40E, Tanaka Kikinzoku Kogyo TKK) were used as received without purification. All syntheses were carried out under Ar(g) using standard Schlenk techniques, and workup procedures were performed in air. Electrolyte solutions were prepared with deionized water (resistance: 18.2 MΩ) and potassium hydroxide (KOH, semiconductor grade 99.99%, Alfa Aesar).

Synthesis of PdBi₂ Nanoparticles. In a typical synthesis, 61 mg of Pd(acac)₂ (0.2 mmol), 154 mg of Bi(oac)₃ (0.4 mmol), and 10 mL of OLAM were first added to a 20 mL scintillation vial with a magnetic stir bar. After stirring for 20 min, the vial was sonicated for another 10 min to ensure that all of the solid precursors were dissolved and the mixture formed a pale-yellow solution. Another 5 mL of OLAM was added to a 100 mL three-necked round-bottomed flask with a condenser, thermometer adapter, thermometer, and rubber septum. Magnetic stirring was started, and the solution was degassed under vacuum at 120 $^{\circ}$ C for \sim 5–10 min. The flask was backfilled with Ar and heated to \sim 300 $^{\circ}$ C at a rate of 10 $^{\circ}$ C/min. Once the temperature reached 300 $^{\circ}$ C, the 10 mL of precursor solution was slowly injected into the flask using a syringe pump at a rate of 0.3 mL/min. The solution in the flask turned from colorless to light brown and finally formed a dark-brown colloidal mixture when the injection was completed. The solution was then rapidly cooled by removing the flask from the heating mantle. The NPs were precipitated by adding 10 mL of ethanol and then centrifuged at 8000 rpm for 5 min. The precipitate was washed three times using a 1:1 ethanol/toluene mixture (with centrifugation in between washes) and could then be suspended in ethanol for further characterization and electrode preparation.

Physicochemical Characterization. The ethanol suspension of the NPs was dropcasted onto a zero-background Si wafer substrate and examined with a Philips X'Pert Pro Powder X-ray diffractometer (XRD) with CuK radiation ($K\alpha_1$, $\lambda=1.5406$ Å; $K\alpha_2$, $\lambda=1.5444$ Å). Transmission electron microscopy (TEM) was performed on an FEI F200C Talos or an FEI Tecnai TF30 operation at 200 kV. The materials on the glassy carbon disk after the electrochemical test were dissolved by concentrated nitric acid and then diluted with water. The metal concentration in the nitric acid solution was analyzed by the PerkinElmer NexION 300D with ICP.

Oxygen Reduction Measurements. Electrochemical measurements were carried out with a potentiostat/galvanostat (Metrohm Autolab Potentiostat or Nuvant EzStat Pro) and a three-electrode Teflon cell with 0.1 M KOH aqueous solution as the electrolyte. A Hg/HgO electrode in 1 M NaOH was used as the reference electrode. A graphite rod was used as the counter electrode. The Hg/HgO reference electrode was periodically checked with an RHE to verify the stability of the reference potential. All data were measured with IR compensation on the potentiostat. The ORR was performed by sweeping the voltage from -0.9 to 0.2 V vs Hg/HgO at a sweep rate of 20 mV/s or by constant potential chronoamperometery within the same potential range. All measurements were performed on a 5 mm diameter rotating disk electrode (RDE) at 1600 rpm. All ORR measurements were IR-corrected, and the IR drop was measured by the positive feedback or current interrupt method.

CO Stripping Measurements. We utilized the CO stripping method to determine the electrochemically active surface area (ECSA) of Pt or Pd atoms on the surface of the electrode. The electrodes were first held at 0.15 V vs RHE for 20 min in 0.1 M KOH saturated with CO to form a surface-adsorbed CO monolayer, followed by the removal of

CO(aq) by saturating the electrolyte with Ar for 15 min. Finally, the voltage was swept from 0.15 to 1.15 V vs RHE to oxidize the adsorbed CO layer. The surface area of the sample could be calculated by integrating the oxidation peak, assuming one CO adsorbed per Pd or Pt atom on the surface. The ratio of charge transferred for the CO oxidation and metal surface area was estimated to be $484\,\mu\text{C/cm}^2$ for Pt and $420\,\mu\text{C/cm}^2$ for Pd and Pd₃Bi. We expect that Bi sites will not adsorb CO; therefore, CO stripping will not account for catalytically inactive Bi sites on the surface.

Conversion of PdBi₂ to Pd₃Bi. The electrode was prepared by directly dropcasting 4 μ L of the ethanol suspension of the as-prepared NP onto the glassy carbon disk. After it dried out, the electrode was then immersed in 0.1 M acetic acid solution for 20 min, followed by DI water wash, acetone wash, and ethanol wash. Finally, the electrode was placed in a UV-ozone chamber and treated with UV and ozone at room temperature for 20 min. A graphite rod and Hg/HgO electrode were used as the counter and reference electrodes, respectively. The working electrode was then conditioned by cycling the potential from -0.9 to 0.2 V vs Hg/HgO reference at a scan rate of 0.1 V s⁻¹ and at a rotation rate of 1600 rpm for ~ 500 cycles.

Preparation of Pt/C and Pd/C Electrodes. To prepare Pd/C materials, 30 mg of 40% Pd on Vulcan XC 72 (Premetek) was dispersed into a solution consisting of a mixture of 8 μ L of Nafion ionomer, 1 mL of DI water, and 1 mL of IPA. The resulting solution was sonicated for 20 min. 1 μ L of the mixture was dropcasted onto the 5 mm diameter disk. The Pt/C sample was prepared with the same procedure except with Pt/C (TKK).

Sample Preparation for ICP-MS Analysis. After the electrochemical measurement, the glassy carbon electrode was taken out of the electrolyte and rinsed with 18.2 M Ω water. After it was dried in air, the electrode was placed in a plastic tube, and 1 mL of concentrated tracemetal-grade nitric acid was added to the tube. The tube was sonicated for a few minutes to fully dissolve the catalyst on the surface. An additional 9 mL of 18.2 M Ω water was added to the tube, and the solution was ready for testing.

Computational Methods. The Pourbaix diagrams were generated using PyMatGen with data provided by the Materials Project. ⁴³ To best view the possible formation of solid-state phases, the concentrations of aqueous species in the Pourbaix diagrams were set to the upper limit that could be achieved if all PdBi₂ were dissolved. Because it is now believed that the aqueous species previously identified as BiO⁺ is in fact $\mathrm{Bi_6O_4(OH)_4^{6+}}$, the labels on the generated Pourbaix diagram have been changed accordingly. ³¹

XPS Analysis. Binding energies have been corrected by shifting the peak of C 1s to 284.8 eV. Palladium peak positions have been assigned according to the values in the *Handbook of X-ray Photoelectron Spectroscopy* and reported data in NIST database, whereas Bi peak positions have been assigned according to the values of Casella and Contursi. The splitting of peaks usually occurs asymmetrically for metals in their lowest oxidation state and mostly symmetrically for higher oxidation states, and the symmetry of peaks is controlled by the peak area. The fwhm is assumed to be in the range of 0.9 to 1.1 eV for metals and in the range of 1.7 to 2.0 for oxides. To properly fit the spectra, the separation between the peaks is set to 5.2 and 5.3 eV for Pd and Bi, respectively. By utilizing relative sensitivity factors (RSFs), the peak areas of the Pd and Bi are corrected, and their ratio is calculated to yield the surface atomic ratio as

$$surface \ atomic \ ratio = \frac{region \ peak \ area_{p_d}/RSF_{p_d}}{region \ peak \ area_{p_i}/RSF_{Bi}}$$

ASSOCIATED CONTENT

S Supporting Information

The Supporting Information is available free of charge on the ACS Publications website at DOI: 10.1021/acsnano.9b06019.

Details of the structural characterization, electrochemistry, and XPS analysis (PDF)

AUTHOR INFORMATION

Corresponding Author

*E-mail: shoji@jhu.edu.

ORCID

Kenneth J.T. Livi: 0000-0001-7728-5460 Chenyang Li: 0000-0002-5155-4631 Anthony Shoji Hall: 0000-0003-4134-4160

Author Contributions

D.S. and Y.W. are cofirst authors.

Notes

The authors declare no competing financial interest.

This manuscript was also submitted to the ChemRxiv preprint server before submission to this journal (Sun, D.; Wang, Y.; Livi, K. J. T.; et al. Ordered Intermetallic Nanoparticles with High Catalytic Activity Prepared by an Electrochemically Induced Phase Transformation. **2019**, *ChemRxiv* 8289812. https://doi.org/10.26434/chemrxiv.8289812.v1 (accessed 19 Jun, 2019)).

ACKNOWLEDGMENTS

A.S.H. acknowledges financial support from the National Science Foundation under award no. CHE-1764310 and the Johns Hopkins University Catalyst award. T.M. acknowledges financial support from the National Science Foundation under award no. CHE-1437396. Computational resources were provided by the Maryland Advanced Research Computing Center (MARCC) and Homewood High-Performance Cluster (HHPC) at Johns Hopkins University. We gratefully acknowledge Prof. Mingwei Chen (JHU) and Prof. Jonah Erlebacher (JHU) for helpful discussions.

REFERENCES

- (1) Coleman, E. J.; Chowdhury, M. H.; Co, A. C. Insights Into the Oxygen Reduction Reaction Activity of Pt/C and PtCu/C Catalysts. *ACS Catal.* **2015**, *5*, 1245–1253.
- (2) Mukerjee, S.; Srinivasan, S.; Soriaga, M. P.; McBreen, J. Role of Structural and Electronic Properties of Pt and Pt Alloys on Electrocatalysis of Oxygen Reduction: An *In Situ* XANES and EXAFS Investigation. *J. Electrochem. Soc.* **1995**, *142*, 1409–1422.
- (3) Casado-Rivera, E.; Volpe, D. J.; Alden, L.; Lind, C.; Downie, C.; Vázquez-Alvarez, T.; Angelo, A. C. D.; DiSalvo, F. J.; Abruña, H. D. Electrocatalytic Activity of Ordered Intermetallic Phases for Fuel Cell Applications. *J. Am. Chem. Soc.* **2004**, *126*, 4043–4049.
- (4) Wang, D.; Xin, H. L.; Hovden, R.; Wang, H.; Yu, Y.; Muller, D. A.; DiSalvo, F. J.; Abruña, H. D. Structurally Ordered Intermetallic Platinum—Cobalt Core—Shell Nanoparticles with Enhanced Activity and Stability As Oxygen Reduction Electrocatalysts. *Nat. Mater.* **2013**, *12*, 81–87.
- (5) Wencka, M.; Hahne, M.; Kocjan, A.; Vrtnik, S.; Koželj, P.; Korže, D.; Jagličić, Z.; Sorić, M.; Popčević, P.; Ivkov, J.; Smontara, A.; Gille, P.; Jurga, S.; Tomeš, P.; Paschen, S.; Ormeci, A.; Armbrüster, M.; Grin, Y.; Dolinšek, J. Physical Properties of the InPd Intermetallic Catalyst. *Intermetallics* **2014**, *55*, 56–65.
- (6) Cui, Z.; Chen, H.; Zhao, M.; DiSalvo, F. J. High-Performance Pd₃Pb Intermetallic Catalyst for Electrochemical Oxygen Reduction. *Nano Lett.* **2016**, *16*, 2560–2566.
- (7) Yan, Y.; Du, J. S.; Gilroy, K. D.; Yang, D.; Xia, Y.; Zhang, H. Intermetallic Nanocrystals: Syntheses and Catalytic Applications. *Adv. Mater.* (Weinheim, Ger.) **2017**, 29, 1605997.
- (8) Teichert, J.; Heise, M.; Chang, J.-H.; Ruck, M. Refinement of the Microwave-Assisted Polyol Process for the Low-Temperature Synthesis of Intermetallic Nanoparticles. *Eur. J. Inorg. Chem.* **2017**, 2017, 4930–4938.

(9) Cable, R. E.; Schaak, R. E. Low-Temperature Solution Synthesis of Nanocrystalline Binary Intermetallic Compounds Using the Polyol Process. *Chem. Mater.* **2005**, *17*, 6835–6841.

- (10) Wang, Y.; Sun, D.; Chowdhury, T.; Wagner, J. S.; Kempa, T. J.; Hall, A. S. Rapid Room-Temperature Synthesis of a Metastable Ordered Intermetallic Electrocatalyst. J. Am. Chem. Soc. 2019, 141, 2342–2347.
- (11) Liao, H.; Zhu, J.; Hou, Y. Synthesis and Electrocatalytic Properties of PtBi Nanoplatelets and PdBi Nanowires. *Nanoscale* **2014**, 6, 1049–1055.
- (12) Ji, X.; Lee, K. T.; Holden, R.; Zhang, L.; Zhang, J.; Botton, G. A.; Couillard, M.; Nazar, L. F. Nanocrystalline Intermetallics on Mesoporous Carbon for Direct Formic Acid Fuel Cell Anodes. *Nat. Chem.* **2010**, *2*, 286–293.
- (13) Chen, H.; Wang, D.; Yu, Y.; Newton, K. A.; Muller, D. A.; Abruña, H.; DiSalvo, F. J. A Surfactant-Free Strategy for Synthesizing and Processing Intermetallic Platinum-Based Nanoparticle Catalysts. J. Am. Chem. Soc. 2012, 134, 18453—18459.
- (14) Qi, Z.; Xiao, C.; Liu, C.; Goh, T. W.; Zhou, L.; Maligal-Ganesh, R.; Pei, Y.; Li, X.; Curtiss, L. A.; Huang, W. Sub-4 nm PtZn Intermetallic Nanoparticles for Enhanced Mass and Specific Activities in Catalytic Electrooxidation Reaction. *J. Am. Chem. Soc.* 2017, 139, 4762–4768.
- (15) Chi, M.; Wang, C.; Lei, Y.; Wang, G.; Li, D.; More, K. L.; Lupini, A.; Allard, L. F.; Markovic, N. M.; Stamenkovic, V. R. Surface Faceting and Elemental Diffusion Behaviour at Atomic Scale for Alloy Nanoparticles During *in situ* Annealing. *Nat. Commun.* **2015**, *6*, 8925.
- (16) Kaiser, H. Selective Dissolution of High and Low Diffusivity Alloys—A Comparison of Kinetical and Micromorphological Aspects. *Corros. Sci.* **1993**, *34*, 683–699.
- (17) Marshakov, I. K. Anodic Dissolution and Selective Corrosion of Alloys. *Prot. Met.* **2002**, *38*, 118–123.
- (18) Chen, Q.; Sieradzki, K. Spontaneous Evolution of Bicontinuous Nanostructures in Dealloyed Li-based Systems. *Nat. Mater.* **2013**, *12*, 1102.
- (19) Geng, K.; Liu, M.; Xie, Y.; Aiello, A.; Karasz, E.; Sieradzki, K. Morphology Evolution during Delithiation of Li-Pb Alloys: Oscillatory Electrochemical Behavior. *J. Electrochem. Soc.* **2019**, *166*, C108–C114.
- (20) Wang, D.; Yu, Y.; Zhu, J.; Liu, S.; Muller, D. A.; Abruña, H. D. Morphology and Activity Tuning of Cu₃Pt/C Ordered Intermetallic Nanoparticles by Selective Electrochemical Dealloying. *Nano Lett.* **2015**, *15*, 1343–1348.
- (21) Oezaslan, M.; Hasché, F.; Strasser, P. Pt-Based Core-Shell Catalyst Architectures for Oxygen Fuel Cell Electrodes. *J. Phys. Chem. Lett.* **2013**, *4*, 3273–3291.
- (22) Sun, K.; Cheng, T.; Wu, L.; Hu, Y.; Zhou, J.; Maclennan, A.; Jiang, Z.; Gao, Y.; Goddard, W. A.; Wang, Z. Ultrahigh Mass Activity for Carbon Dioxide Reduction Enabled by Gold–Iron Core–Shell Nanoparticles. *J. Am. Chem. Soc.* **2017**, *139*, 15608–15611.
- (23) Medasani, B.; Haranczyk, M.; Canning, A.; Asta, M. Vacancy Formation Energies in Metals: A Comparison of MetaGGA with LDA and GGA Exchange—Correlation Functionals. *Comput. Mater. Sci.* **2015**, *101*, 96–107.
- (24) Otake, S.; Ishii, Y.; Matsuno, N. Migration Energy of Vacancies in Bismuth. *Jpn. J. Appl. Phys.* **1981**, *20*, 1037–1040.
- (25) Liao, H.; Hou, Y. Liquid-Phase Templateless Synthesis of Pt-on-Pd0.85Bi0.15 Nanowires and PtPdBi Porous Nanoparticles with Superior Electrocatalytic Activity. *Chem. Mater.* **2013**, 25, 457–465.
- (26) Naohara, H.; Ye, S.; Uosaki, K. Thickness Dependent Electrochemical Reactivity of Epitaxially Electrodeposited Palladium Thin Layers on Au(111) and Au(100) Surfaces. *J. Electroanal. Chem.* **2001**, *500*, 435–445.
- (27) Hu, J.-W.; Li, J.-F.; Ren, B.; Wu, D.-Y.; Sun, S.-G.; Tian, Z.-Q. Palladium-Coated Gold Nanoparticles with a Controlled Shell Thickness Used as Surface-Enhanced Raman Scattering Substrate. *J. Phys. Chem. C* **2007**, *111*, 1105–1112.
- (28) Sun, D.; Feng, S.; Terrones, M.; Schaak, R. E. Formation and Interlayer Decoupling of Colloidal MoSe2 Nanoflowers. *Chem. Mater.* **2015**, 27, 3167–3175.

- (29) Sun, Y.; Wang, Y.; Sun, D.; Carvalho, B. R.; Read, C. G.; Lee, C.-h.; Lin, Z.; Fujisawa, K.; Robinson, J. A.; Crespi, V. H.; Terrones, M.; Schaak, R. E. Low-Temperature Solution Synthesis of Few-Layer 1T '-MoTe2 Nanostructures Exhibiting Lattice Compression. *Angew. Chem., Int. Ed.* **2016**, *55*, 2830–2834.
- (30) Parija, A.; Waetzig, G. R.; Andrews, J. L.; Banerjee, S. Traversing Energy Landscapes Away from Equilibrium: Strategies for Accessing and Utilizing Metastable Phase Space. *J. Phys. Chem. C* **2018**, 122, 25709–25728.
- (31) Wiberg, E.; Wiberg, N.; Holleman, A. F. *Inorganic Chemistry*; Academic Press: San Diego, CA, 2001.
- (32) Kohn, W.; Sham, L. J. Self-Consistent Equations Including Exchange and Correlation Effects. *Phys. Rev.* **1965**, *140*, A1133–A1138.
- (33) Henkelman, G.; Jonsson, H. Improved Tangent Estimate in the Nudged Elastic Band Method for Finding Minimum Energy Paths and Saddle Points. *J. Chem. Phys.* **2000**, *113*, 9978–9985.
- (34) Henkelman, G.; Uberuaga, B. P.; Jonsson, H. A Climbing Image Nudged Elastic Band Method for Finding Saddle Points and Minimum Energy Paths. *J. Chem. Phys.* **2000**, *113*, 9901–9904.
- (35) Vineyard, G. H. Frequency Factors and Isotope Effects in Solid State Rate Processes. *J. Phys. Chem. Solids* **1957**, *3*, 121–127.
- (36) Zheng, J.-J.; Margine, E. R. Electron-Phonon Coupling and Pairing Mechanism in β -Bi₂Pd Centrosymmetric Superconductor. *Phys. Rev. B: Condens. Matter Mater. Phys.* **2017**, 95, 014512.
- (37) Jiang, L.; Hsu, A.; Chu, D.; Chen, R. Oxygen Reduction Reaction on Carbon Supported Pt and Pd in Alkaline Solutions. *J. Electrochem. Soc.* **2009**, *156*, B370–B376.
- (38) Wang, H.; Luo, W.; Zhu, L.; Zhao, Z.; E, B.; Tu, W.; Ke, X.; Sui, M.; Chen, C.; Chen, Q.; Li, Y.; Huang, Y. Synergistically Enhanced Oxygen Reduction Electrocatalysis by Subsurface Atoms in Ternary PdCuNi Alloy Catalysts. *Adv. Funct. Mater.* **2018**, 28, 1707219.
- (39) Sekol, R. C.; Li, X.; Cohen, P.; Doubek, G.; Carmo, M.; Taylor, A. D. Silver Palladium Core—Shell Electrocatalyst Supported on MWNTs for ORR in Alkaline Media. *Appl. Catal., B* **2013**, *138*, 285–293.
- (40) Heinzel, A.; Barragán, V. M. A Review of the State-of-the-Art of the Methanol Crossover in Direct Methanol Fuel Cells. *J. Power Sources* **1999**, *84*, 70–74.
- (41) Ataee-Esfahani, H.; Wang, L.; Nemoto, Y.; Yamauchi, Y. Synthesis of Bimetallic Au@Pt Nanoparticles with Au Core and Nanostructured Pt Shell toward Highly Active Electrocatalysts. *Chem. Mater.* **2010**, *22*, 6310–6318.
- (42) Gurau, B.; Smotkin, E. S. Methanol Crossover in Direct Methanol Fuel Cells: A Link between Power and Energy Density. *J. Power Sources* **2002**, *112*, 339–352.
- (43) Persson, K. A.; Waldwick, B.; Lazic, P.; Ceder, G. Prediction of Solid-Aqueous Equilibria: Scheme to Combine First-Pinciples Calculations of Solids with Experimental Aqueous States. *Phys. Rev. B: Condens. Matter Mater. Phys.* **2012**, 85, 235438.
- (44) Wagner, C. Handbook of X-ray Photoelectron Spectroscopy: A Reference Book of Standard Data for Use in X-Ray Photoelectron Spectroscopy; Perkin-Elmer: Eden Prairie, MN, 1979.
- (45) Casella, I.; Contursi, M. Characterization of Bismuth Adatom-Modified Palladium Electrodes. *Electrochim. Acta* **2006**, *52* (2), 649–657.